Trans. Japan Soc. Aero. Space Sci.
Vol. 53, No. 180, pp. 122–129, 2010

Novel Flow Control Method for Vortex Shedding of Turbine Blade

By Mahmoud M. EL-GENDI,[1)] Mohammed K. IBRAHIM,[1),2)] Koichi MORI[1)] and Yoshiaki NAKAMURA[1)]

[1)]*Department of Aerospace Engineering, Nagoya University, Nagoya, Japan*
[2)]*Aerospace Engineering Department, Faculty of Engineering, University of Cairo, Giza, Egypt*

(Received May 11th, 2009)

Three-dimensional flow simulations through a turbine cascade were carried out for an exit isentropic Mach number of 0.79 and a Reynolds number of 2.8×10^6. The main objective is to increase the base pressure. Calculations were carried out using an in-house numerical code, where a 2nd order Roe's flux-difference splitting for inviscid numerical fluxes, a 2nd order implicit dual time method for time integration, and Delayed Detached Eddy Simulation for turbulence were employed. The present idea to increase the base pressure is to connect the pressure and suction sides of the blade using microtubes distributed uniformly along the span on the trailing edge. Simulated results show that this modification does not affect the blade load, increases the base pressure by 0.7%, and decreases the overall loss by 3%.

Key Words: Vortex Shedding, CFD, Microtubes, Turbine Blade, Flow Control

1. Introduction

The main target of turbomachinery designers is increasing the efficiency by decreasing the loss of energy. Any reduction of efficiency caused by flow is termed loss. The base pressure plays a vital role in the trailing edge (TE) loss, which contributes one-third of total loss.[1)]

Flow control can increase the base pressure and improve the turbine efficiency.[2)] Choi et al.[3)] reviewed most flow control methods over a blunt body under three main categories: passive, active open-loop, and active feedback control methods. El-Gendi et al.[4,5)] controlled the flow passively through a turbine cascade using an elliptic trailing edge instead of a circular one. For active open-loop control methods, Kim and Choi[6)] studied the effect of sinusoidal blowing-and-suction along a circular cylinder span. Park et al.[7)] investigated the effect of a feedback sensor location in the wake of the controlled flow using blowing-and-suction slots. Min and Choi[8)] tried to minimize the difference between instantaneous surface pressure and potential pressure through blowing-and-suction on the cylinder surface as a suboptimal feedback control method. Delaying the separation by synthetic jet,[9)] plasma actuator,[10,11)] surface roughness,[12)] separation and reattachment,[13)] or vortex generator jets[14–17)] are successful tools in flow control. Flow control methods are not exclusive on the body surface; flow can be controlled by controlling the wake through splitter plate,[18)] base blowing-and-suction,[19)] or small control cylinder.[20)]

Cicatelli and Sieverding[21)] advocated that the vortex shedding evolution needs more investigation. Regarding this issue, Desse[22)] conducted an experiment for flat plates, and Cicatelli and Sieverding[23)] considered a turbine cascade with exit isentropic Mach number, $M_{2,\mathrm{is}}$, of 0.4. Sondak and Dorney[24)] and Cicalelli et al.[25)] numerically investigated this problem by using the same cascade and flow conditions as Cicatelli and Sieverding.[23)] Sieverding et al.[26,27)] experimentally and El-Gendi et al.[28)] numerically investigated the vortex shedding evolution process at $M_{2,\mathrm{is}} = 0.79$ on a blade with half the scale of that used in other research.[23–25,29)]

So far, passive and active feedback control methods are distinct approaches. In this study, we perform a numerical simulation for the experimental results of Sieverding et al.[26,27)] Based on our understating of the vortex evolution process and our numerical results, we propose a new, hybrid flow control method. In this method, the TE geometry is modified by connecting the pressure and suction sides by equidistant microtubes along the span near the start of the trailing edge. This method is a hybrid between passive and active feedback methods. It has the advantage of a passive control method because it is a trailing edge modification so it is practical. Also, it has the advantage of an active feedback control method because it takes feedback from the flow and accordingly changes its action.

2. Study Models

Two test cases were investigated: a baseline case (BC), and modified case (MC). The turbine cascade of both cases is the same as that used in Sieverding et al.[26,27)] The VKI blade profile and turbine cascade are shown in Fig. 1; the cascade dimensions are presented in Table 1, and TE in MC is highlighted in Fig. 2.

The BC is the same as that used by Sieverding et al.[26,27)] On the other hand, the MC has microtubes connecting the pressure and suction sides at $S/D \approx \pm 0.66$. The reason for choosing this location is discussed in section 4.1. As shown in Fig. 2, the abscissa "S" represents the length along the circular trailing edge surface, where the negative sign refers to the direction from the trailing edge center ($S = 0$) toward the pressure surface, and the positive sign refers toward the

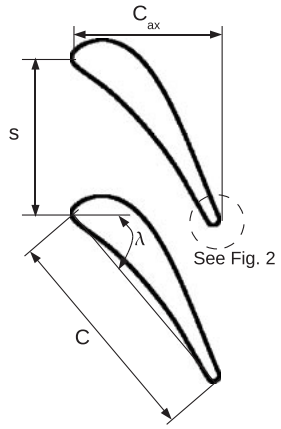

Fig. 1. Turbine cascade.

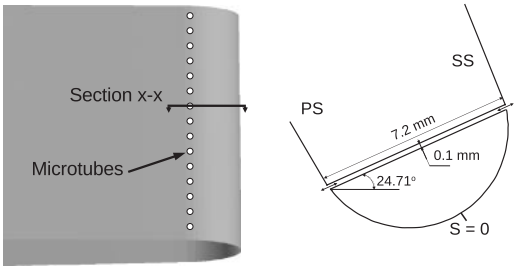

(a) perspective view (b) section x-x

Fig. 2. Location of microtubes; not to scale.

Table 1. Dimensions of cascades.

Name	Symbol	Dimension	Unit
Chord	C	140.00	mm
Axial chord	C_{ax}	91.84	mm
Pitch	s	97.44	mm
TE thickness	D	7.43	mm
TE wedge angle	δ_{te}	7.50	degree
Stagger angle	λ	49.83	degree

suction surface, and D is the trailing edge thickness. PS refers to the pressure side and SS the suction side. In the computational domain, along the span, there are 50 microtubes. Every microtube has a radius ($R = 0.05$ mm) and length ($L = 7.2$ mm) and is inclined to the x-axis by 24.71° (Fig. 2). The distance between the centerlines of successive microtubes is 0.3 mm.

3. Numerical Methods

3.1. Computational grid

Figure 3 shows an O-type grid used in the present calculations for both cases. The grid has $413 \times 194 \times 50$ grid points with an approximate total grid points of 4.0×10^6. The minimum grid size is 0.002 mm, which is equivalent to $y^+ \approx 1$. Because the turbine blade has round leading and trailing edges, the O-type grid is used in this study to reduce grid skewness near TE as shown in Fig. 3. The grid

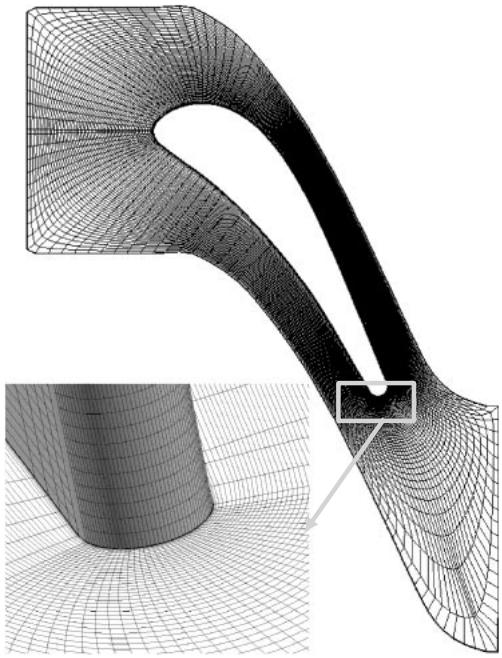

Fig. 3. Computational grid; each third line is rendered.

spacing along the span direction is equidistant ($\Delta z = 0.3$ mm). The computational domain span height (Λ_z) is 14.7 mm, which is approximately twice the trailing edge thickness ($\Lambda_z \approx 2D$) and one-tenth the chord ($\Lambda_z \approx 0.1C$).

3.2. Boundary conditions

3.2.1. General conditions

Both baseline and modified cases have the same boundary conditions as Sieverding et al.[26] At inlet, the total pressure ($P_{o1} = 140$ kPa) and the total temperature ($T_{o1} = 280$ K) are imposed, whereas at exit, the static pressure ($P_2 = 92{,}755$ Pa) is imposed. According to these boundary conditions, the exit isentropic Mach number ($M_{2,is}$) is 0.79 and the exit isentropic Reynolds number ($Re_{2,is}$), based on the chord, is 2.8×10^6. In actual simulation, the inlet and exit boundary conditions were calculated using the method of characteristics. No slip and adiabatic boundary conditions were implemented along the solid wall. A periodic condition was used in both pitch and span directions.

3.2.2. Numerical conditions for microtubes

In the MC, because the microtubes have a microscopic radius ($R = 0.05$ mm) and it is difficult to simulate flows through them, we assume Hagen-Poiseuille flows through the microtubes. We assume that every grid point in the span direction is located at a microtube's centerline and the velocity through each microtube is calculated by the following relation:

$$U = \frac{R^2}{4\mu}\left(-\frac{\Delta P}{\Delta L}\right)$$

where, R is the microtube radius ($R = 0.05$ mm), ΔL is the microtube length ($\Delta L = 7.2$ mm), μ is the flow absolute viscosity, and ΔP is the pressure difference across the microtube. The suction and injection flow angles on both PS and SS are the same as the microtube angle with x-axis.

During this modeling, attention was given to mass, momentum, and energy conservation. Also, we assume that the flow through the microtubes is laminar, incompressible, fully developed, and steady. It is worth mentioning that this modeling may augment or degrade a physical microtube effect.

3.3. Numerical scheme

Calculations were carried out using a parallel, inhouse, structure, single-block code, where the Navier-Stokes equations were discretized by the cell vertex method. In this code, the lower upper symmetric Gauss Seidel (LUSGS) method was used along with the dual-time method to obtain time accurate results for unsteady calculations. In addition, Roe's flux-difference splitting with E-fix was used to calculate inviscid numerical fluxes, where the second-order accuracy was achieved by the MUSCL scheme with the Van Albada flux limiter. On the other hand, viscous fluxes were calculated by central difference.

The calculations were carried out by an eight-processor Linux cluster. To accelerate simulation, we began calculations as a two-dimensional calculations using three grid points in span-wise direction. The two-dimensional calculations took about 4 hours to reach a fully developed state. The output of the two-dimensional calculations was taken as the initial condition for three-dimensional calculations. To include the three-dimensional effect in time-average results, a time-average counter was switched on after 2000 iterations and switched off at 12000 iterations. This process took about 70 hours. Every iteration has five inner iterations for the implicit scheme (time marching), a dimensionless time step, $\Delta t^* = 105.42 \times 10^{-6}$, and a physical time step, $\Delta t = 3.33 \times 10^{-7}$ s, which is equivalent to CFL ≈ 100. We think these numbers of iterations were sufficient because we increased the numbers, and found no significant discrepancy in the results. Instantaneous results were calculated at CFL ≈ 10.

3.4. Turbulence model

The Delayed Detached Eddy simulation (DDES[30]) method was used as a turbulent model. It is a hybrid scheme that works as a Reynolds Average Navier-Stokes (RANS) model near the wall and as a Large Eddy Simulation (LES) model away from the wall. Unlike RANS models, DDES can provide more accurate results for unsteady flows. Unlike LES, DDES does not require a very fine grid near the wall. To estimate the boundary layer region where RANS is applied, DDES depends on flow and grid spacing instead of only on grid spacing, so DDES has an advantage over Detached Eddy Simulation (DES).

4. Results and Discussion

4.1. Vortex shedding mechanism of BC

Figure 4 shows flow quantities of BC in the circular TE region during one vortex cycle period, T, where $t = 0T$ and $t = T$ are approximately the same phase. Figures 4(a), (b), (c), and (d) represent dimensionless vorticity contours, density gradient contours, pressure contours, and pressure distribution, respectively (see Appendix).

Figure 4 shows that free shear layers play the role of tuning fork tines, where the tines move and push air particles outward so there is compression. Then, the tines move back so there is rarefaction. Pressure waves are formed by these compressions and rarefactions.

At $t = 0T$, the vortex on the PS is at the end of its separation phase and the free shear layer is at the outermost location, but the vortex on the SS is in its formation phase and the free shear layer moves back as shown in Fig. 4(a). Because the shear layer is outer-most, compression near the PS reaches its peak as shown in Fig. 4(b). The refraction near the SS is toward its peak because the SS shear layer is toward its innermost location. The pressure wave resulting from the compression process begins to separate from the trailing edge as shown in Fig. 4(c) because the compression reaches its peak near the PS. At this instant, the pressure on the PS reaches its maximum value and the pressure on the SS is toward its minimum value (Fig. 4(d)).

At $t = 0.08T$, the free shear layer on the PS moves back, but on the SS reaches its innermost location as shown in Fig. 4(a). There is rarefaction near the PS, and rarefaction near the SS reaches its peak (Fig. 4(b)). The pressure wave separates from the PS and moves upstream toward SS of the neighbor blade as shown in Fig. 4(c). As shown in Fig. 4(d), pressure on the PS decreases and reaches its minimum value on the SS.

At $t = 0.45T$, the situation on the PS and SS is opposite to that at $t = 0T$. The free shear layer on the PS moves back, but on the SS reaches its outermost location as shown in Fig. 4(a). There is rarefaction near PS, and compression near SS reaches its peak (Fig. 4(b)). A pressure wave on the SS begins to separate and move upstream as shown in Fig. 4(c). Pressure on the PS decreases, but reaches its maximum value on the SS (Fig. 4(d)).

At $t = 0.6T$, the shear layer on the PS reaches its innermost location, but on the SS moves back (Fig. 4(a)). There is rarefaction near the SS, and rarefaction near the PS reaches its peak, as shown in Fig. 4(b). As shown in Fig. 4(c), the pressure wave separates from the SS and moves upstream. At this moment, the pressure reaches its minimum value on the PS and decreases on the SS as shown in Fig. 4(d).

At $t = 0.85T$, this is an intermediate stage, i.e., the pressure is neither minimum nor maximum on the PS or SS, but its value is minimum at the TE center $(S/D) = 0.0$. The shear layer on the PS moves forth and on the SS moves back as shown in Fig. 4(a). There is compression near the PS and rarefaction near the SS as shown in Fig. 4(b). The pressure wave on the PS develops and moves away from the blade on the SS as shown in Fig. 4(c). The pressure increases on the PS and decreases on the SS as shown in Fig. 4(d).

At $t = T$, the flow quantities are very similar to these at $t = 0T$ and the cycle is completed.

As seen from Fig. 4, although the time average pressure values at $S/D \approx \pm 0.66$ are very low, the instantaneous values are approximately out-phase, i.e., when the instantaneous pressure at $S/D \approx -0.66$ is very low, its value at

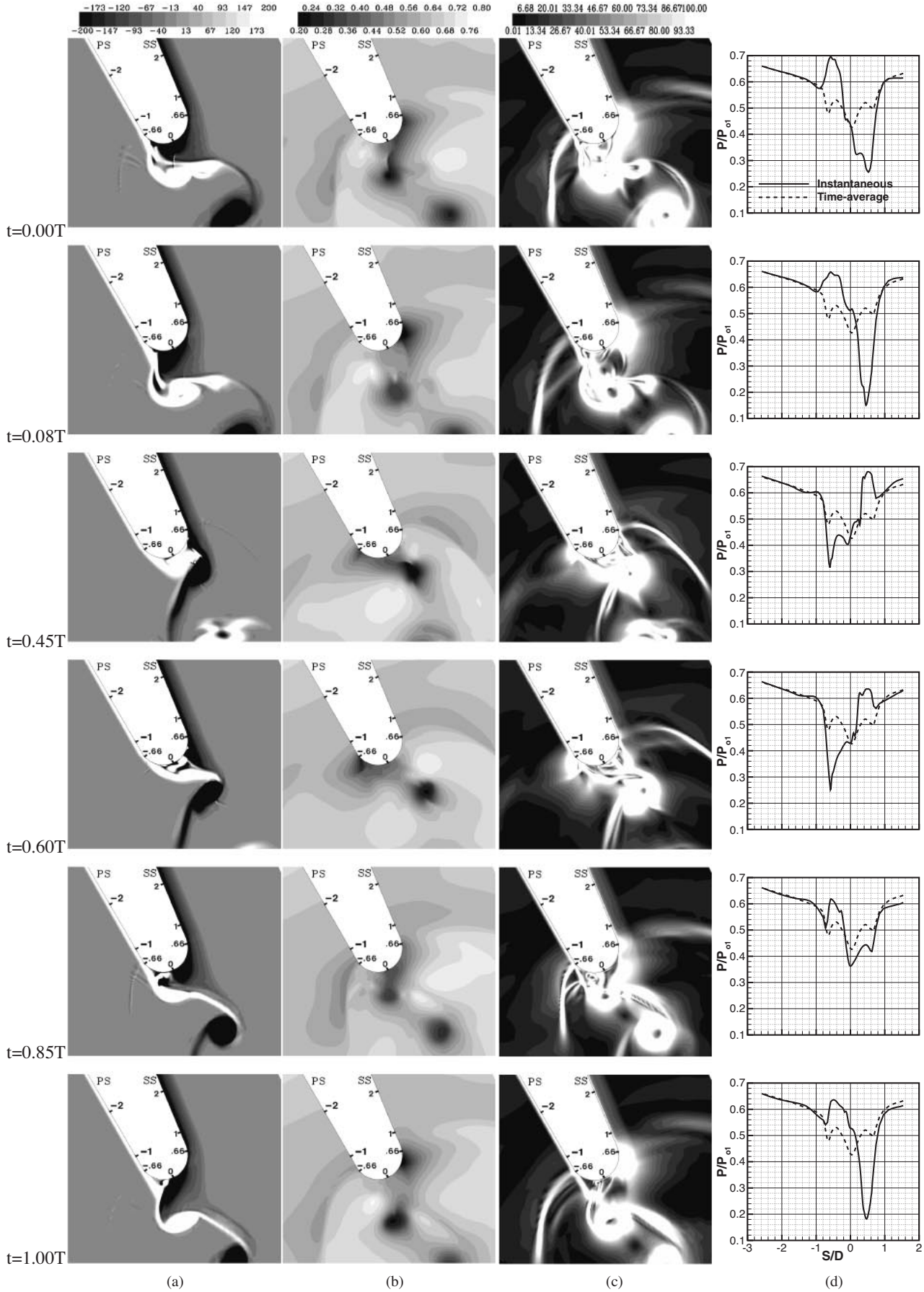

Fig. 4. Dimensionless flow quantities in trailing edge region during one vortex shedding cycle, T: (a) vorticity contours ($\nabla \times \vec{V}/(c_\infty/L)$), (b) density gradient contours ($\nabla\rho/(\rho_\infty/L)$), (c) pressure contours (P/P_{o1}), and (d) pressure distribution (P/P_{o1}).

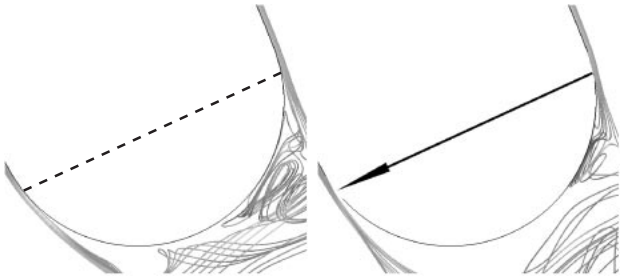

(a) BC (b) MC

Fig. 5. Streamlines at $t = 0.45T$.

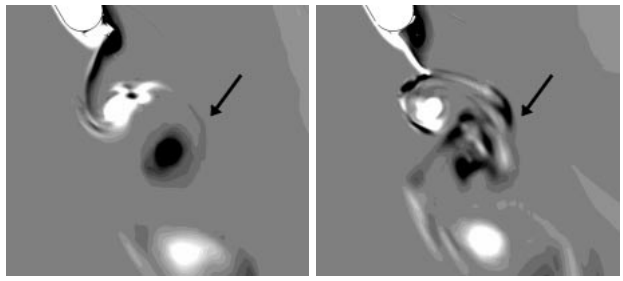

(a) BC (b) MC

Fig. 6. Vorticity contours at $t = 0.45T$.

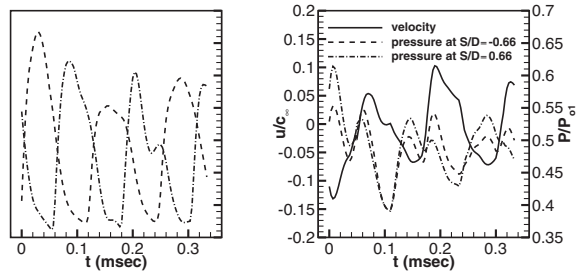

(a) BC (b) MC

Fig. 7. Microtube effect on pressure trace.

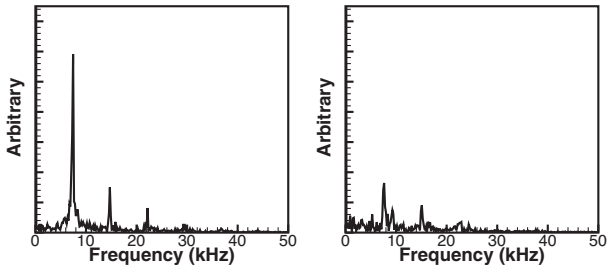

(a) BC (b) MC

Fig. 8. Pressure spectra at $S/D = -0.66$.

$S/D \approx 0.66$ is very high and vice versa. We expect that connecting these regions together disturbs the vortex shedding and redistributes the energy. There are many methods for this connection. In this study, we propose equidistant spanwise microtubes.

4.2. Instantaneous comparison

The mechanism of injection and suction processes

The streamlines for both cases approximately at the same phase ($t = 0.45T$; Fig. 4) at the midspan are shown in Fig. 5. In MC, the arrow indicates the microtube location and its head indicates the flow direction. In BC, the dashed line is drawn for declaration only to simplify the comparison. Because of three-dimensional calculations, the intersection among streamlines is an illusion, i.e., not in the same plane. At this instant of BC ($t = 0.45T$; Fig. 4), pressure increases on the SS and the shear layer is outermost. On the other hand, pressure decreases on the PS and the shear layer is toward the innermost location. Because of the microtubes in MC, bypass flow moves through the microtubes from the high pressure region (on SS) toward the low-pressure region (on PS). This bypass flow creates a flow suction near the high-pressure region (on SS) and hinders the shear layer on the SS to move forth so that it becomes more attached to the blade surface. On the other hand, this bypass flow causes flow injection near the low-pressure region (on PS), pushes the shear layer on the PS a little away, and alleviates its interaction with the shear layer of the SS in the wake region. As shown in Fig. 5, the flow suction at the SS of the MC delays the flow separation.

On other hand, the flow injection at the PS of the MC pushes the free shear a little outward layer and alleviates the interaction between pressure and suction free shear layers in the wake (Fig. 6). The effect of this mechanism in the wake region on the vorticity is shown in Fig. 6. Figure 6 shows that this mechanism affects the coherent structure of the SS vortex in the wake and has a little effect on the PS vortex size.

Feedback and actuation

Figure 7(a) shows the pressure traces at midspan at ($S/D \approx \pm 0.66$) of BC. At the same points, Fig. 7(b) shows the centerline flow quantities of the microtube at the midspan so that the velocity represents the centerline velocity of the microtube and pressure represents the pressure at the microtube ends. As shown in Fig. 7, the pressure signals changed dramatically from approximately out-phase in the BC to approximately in-phase in the MC.

The positive sign of the velocity means there is injection at the SS ($S/D \approx 0.66$) and suction at the PS ($S/D \approx -0.66$), and vice versa. The injection and suction flows take feedback from the pressure across the microtube and continuously change their value and sign as shown in Fig. 7(b). This control method is a hybrid passive and active feedback control method. Like passive methods, it is a modification of TE geometry. Like active feedback methods, it takes feedback from the flow and accordingly changes its action.

Vortex shedding frequency

Spectral analysis was made for the pressure fluctuations at midspan at $S/D = -0.66$ as shown in Fig. 8. The calculations were carried out at CFL ≈ 100. In BC, there is a predominant vortex shedding frequency of 7.45 kHz, which shows reasonable agreement with an experimentally obtained frequency of 7.37 kHz[26] or 7.6 kHz.[27] On the other hand, the predominant vortex shedding frequency of MC is

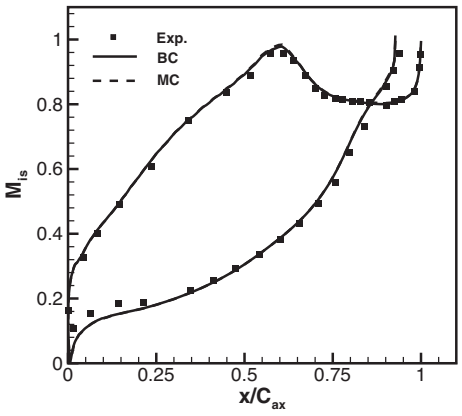

Fig. 9. Isentropic Mach number distribution.

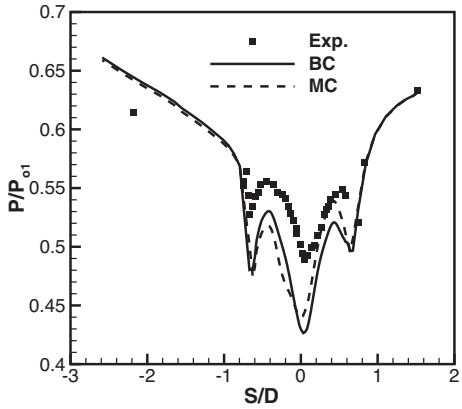

Fig. 10. Distributions of time-average pressure along TE.

Table 2. Boundary layers data.

	PS			SS			
	Exp	BC	MC	Exp	BC	MC	
δ	0.6	0.59	0.59	2.0	2.13	2.13	mm
U_δ		262	263		257	257	m/s
Y_1^+		1.6	1.6		1.4	1.4	
δ^*		0.07	0.07		0.29	0.29	mm
θ		0.05	0.05		0.22	0.22	mm
H	1.53	1.42	1.42	1.31	1.33	1.33	

7.64 kHz. Figure 8 shows that the pressure amplitude of the predominant frequency of MC is lower than that of BC by about 72%, indicating that microtubes dampen the pressure fluctuations of the vortex shedding at $S/D = -0.66$.

4.3. Time-average comparison

Velocity distribution along the blade

Figure 9 shows a time-averaged isentropic Mach number distribution around the blade along with experimental data.[26] The isentropic Mach number on the blade is defined as a function of static pressure on the blade surface and the total pressure at the inlet. The BC numerical results show good agreement with the experimental data. The isentropic Mach number distribution of MC coincides with that of BC, so that our modification in the TE does not affect blade load.

Boundary layers

The comparison between BC, MC, and experimental data[26] is shown in Table 2 at $S/D = \pm 1.75$. These locations are about D upstream of the microtubes, so they can give a good indication about the nature of the boundary layers just before the microtubes.

Table 2 contains the boundary layers data, where δ, U_δ, Y_1^+, δ^*, θ, and H refer to the boundary layer thickness, velocity at boundary layer edge, the dimensionless distance of the first grid point from the wall, displacement thickness, momentum thickness, and shape factor, respectively. There is good agreement between BC and experimental data and shape factor indicates turbulent boundary layers. In addition, the microtubes hardly affected the incoming boundary layer.

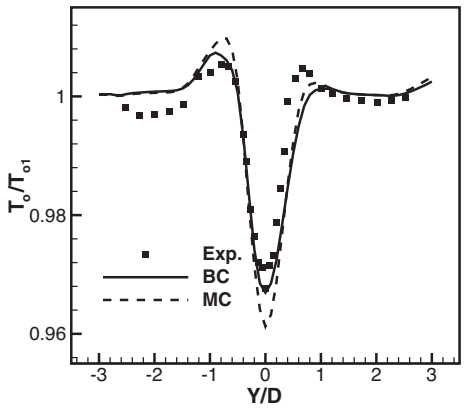

Fig. 11. Eckert-Wiese effect at $X/D = 2.5$.

Pressure along TE

Both time-averaged numerical and experimental[26] pressure distributions normalized by the inlet total pressure, p/p_{o1}, along the TE surface are shown in Fig. 10. The experimental data and numerical results of BC agree qualitatively.

The numerical non-uniform pressure distribution along the TE surface confirms the experimental data.[26] The microtubes in the MC improve the pressure distribution except at $-0.6 < S/D < -0.2$ as shown in Fig. 10. This deterioration might result from different boundary layer characteristics between PS and SS (Table 2). However, the MC increases the average base pressure by 0.7%. We expect that this improvement might be augmented by investigating the effect of some parameters like the injection and suction flow angles at PS and SS, connecting media, or connecting tool size and distribution.

Eckert-Weise effect

In the wake, total temperature splits into hot and cold spots which is known as energy separation (instantaneous) and as the Eckert-Weise effect (time-average). To study the effect of this control method on the Eckert-Weise effect, the time-average total temperature distribution normalized by the total temperature at the inlet, T/T_{o1}, is shown in Fig. 11 at $X/D = 2.5$. The "X" axis is tangential to the camber line at the trailing edge and makes 66° with the cascade

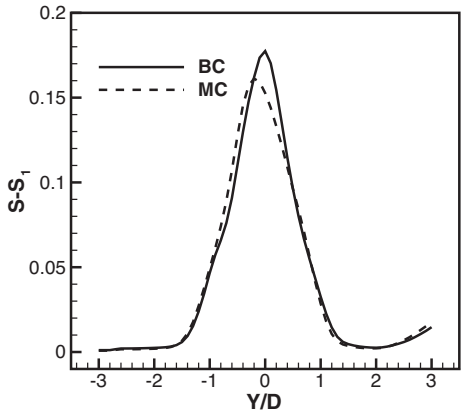

Fig. 12. Entropy distribution at $X/D = 2.5$.

axial direction. The "Y" axis represents the traverse direction and is normal to "X", and the origin of the axes was taken at TE.

As shown in Fig. 11, the numerical results of BC agree well with the experimental data[27] with some discrepancies. The Eckert-Weise effect is observed where the total temperature has low values at the wake middle, exceeds its inlet value at the wake border, and approaches its inlet value in the potential flow region outside the wake. The discrepancy between experimental and numerical results at $Y/D < -1.5$ falls within the probe accuracy.[27] On the other hand, this discrepancy at $Y/D \pm \approx 1$ might be attributed to inability of DDES to capture the effect of small turbulent scales with this grid number. As shown in Fig. 11, the total temperature of MC is lower at the wake centerline and higher at the wake edge than that of BC, so the Eckert-Wiese effect of MC is slightly stronger than that at BC.

Losses

Since entropy represents loss,[1] Fig. 12 shows the comparison of entropy distribution at $X/D = 2.5$ between the two cases. The MC has lower loss than BC in the wake center region and approximately the same outside this region (Fig. 12).

In addition, entropy was estimated at the exit plane (S2–S1) as time, pitchwise, spanwise average. We found that the overall loss of MC (S2–S1 = 19.53 J/kg/K) is 3% lower than that of BC (S2–S1 = 20.23 J/kg/K).

5. Conclusion

Flows through a turbine cascade were numerically simulated for an exit isentropic Mach number of 0.79 and a Reynolds number of 2.8×10^6 using DDES. The present numerical results were compared with the experimental data of Sieverding et al.[26,27] and showed good agreement. Based on our understanding of vortex shedding and evolution processes and our numerical results, we proposed a new, practical shape for the TE to increase the base pressure. In this shape, the PS and SS are connected by equidistant microtubes along the span next to the start of the trailing edge. Flows through these microtubes were modeled as Hagen-Poiseuille flow, which may augment or degrade the physical microtube effect. This TE shape is a hybrid of passive and active feedback control methods. Our modification to the TE geometry changes the pressure traces across the trailing edge from out-phase to in-phase and dampens their fluctuations. Moreover, it maintains the same blade load as the original circular TE geometry, increases the base pressure by 0.7%, and decreases the overall loss by 3%.

Acknowledgments

The first author's Ph.D. program is financially supported by the Egyptian Ministry of Higher Education. We would like to thank Prof. Sieverding who kindly supplied the blade coordinates. We are also grateful to Prof. I. Men'shov for his interesting discussions and fruitful advice.

References

1) Denton, J. D.: Loss Mechanisms in Turbomachines, *ASME J. Turbomach.*, **115** (1993), pp. 621–656.
2) Lord, W. K.: Flow Control Opportunities in Gas Turbine Engines, AIAA Paper 2000-2234, Fluids Conference and Exhibit, 2000.
3) Choi, H., Jeon, W. and Kim, J.: Control of Flow over a Bluff Body, *Annu. Rev. Fluid Mech.*, **40** (2008), pp. 113–139.
4) El-Gendi, M. M., Ibrahim, M. K., Mori, K. and Nakamura, Y.: Elliptic Trailing Edge for a High Subsonic Turbine Cascade, Proceedings of KSAS-JSASS Joint International Symposium on Aerospace Engineering, 2008, pp. 38–42.
5) El-Gendi, M. M., Ibrahim, M. K., Mori, K. and Nakamura, Y.: Effect of Trailing Edge Geometry on a Turbine Blade Base Pressure, Proceedings of International Symposium on Frontiers of Computational Science, 2008, pp. 197–204.
6) Kim, J. and Choi, H.: Distributed Forcing of Flow over a Circular Cylinder, *Phys. Fluids.*, **17** (2005), No. 033103.
7) Park, D. S., Ladd, D. M. and Hendricks, E. W.: Feedback Control of von Kármán Vortex Shedding behind a Circular Cylinder at Low Reynolds Numbers, *Phys. Fluids*, **6** (1994), pp. 2390–2405.
8) Min, C. and Choi, H.: Suboptimal Feedback Control of Vortex Shedding at Low Reynolds Numbers, *J. Fluid Mech.*, **401** (1999), pp. 123–156.
9) Glezer, A. and Amitay, M.: Synthetic Jets, *Annu. Rev. Fluid Mech.*, **34** (2002), pp. 503–529.
10) Matsuno, T., Ota, K., Kanatani, T. and Kawazoe, H.: Optimal and Robust Design of Plasma Actuator for the Control of a Cylinder Wake, Proceedings of KSAS-JSASS Joint International Symposium on Aerospace Engineering, 2008, pp. 115–119.
11) Huang, J., Corke, T. C. and Thomas, F. O.: Plasma Actuators for Separation Control of Low-Pressure Turbine Blades, *AIAA J.*, **44** (2006), pp. 51–57.
12) Gü, O., Farell, C. and Patel, V.: Surface-Roughness Effects on the Mean Flow Past Circular Cylinders, *J. Fluid Mech*, **98** (1980), pp. 673–701.
13) Jeon, S., Choi, J., Jeon, W., Choi, H. and Park, J.: Active Control of Flow over a Sphere for Drag Reduction at a Subcritical Reynolds Number, *J. Fluid Mech.*, **517** (2004), pp. 113–129.
14) Rizzetta, D. P. and Visbal, M. R.: Numerical Study of Active Flow Control for a Transitional Highly Loaded Low-Pressure Turbine, *ASME J. Fluids Eng.*, **128** (2006), pp. 956–967.
15) Volino, R. J.: Separation Control on Low-Pressure Turbine Airfoils Using Synthetic Vortex Generator Jets, *ASME J. Turbomach.*, **125** (2003), pp. 765–777.
16) Bons, J. P., Reimann, D. and Bloxham, M.: Separated Flow Transition on an LP Turbine Blade with Pulsed Flow Control, *ASME J. Turbomach.*, **130** (2008), No. 021014.
17) Bloxham, M., Reimann, D., Crapo, K., Pluim, J. and Bons, J. P.: Synchronizing Separation Flow Control with Unsteady Wakes in a

Low-Pressure Turbine Cascade, *ASME J. Turbomach.*, **131** (2009), No. 021019.
18) Hwang, J., Yang, K. and Sun, S.: Reduction of Flow-Induced Forces on a Circular Cylinder Using a Detached Splitter Plate, *Phys. Fluids*, **15** (2003), pp. 2433–2436.
19) Arcas, D. R. and Redekopp, L. G.: Aspect of Wake Vortex Control through Base Blowing/Suction, *Phys. Fluids*, **16** (2004), pp. 452–456.
20) Sakamoto, H., Tan, K. and Haniu, H.: An Optimum Suppression of Fluid Forces by Controlling a Shear Layer Separated from a Square Prism, *ASME J. Fluids Eng.*, **113** (1991), pp. 183–189.
21) Cicatelli, G. and Sieverding, C. H.: A Review of the Research on Unsteady Turbine Blade Wake Characteristics, Tech. Rep., AGARD-CP-571, Loss Mechanisms and Unsteady Flows in Turbomachines, Paper 6, 1996.
22) Desse, J.: Effect of Time-Varying Wake Flow Characteristics Behind Flat Plates, *AIAA J.*, **36** (1998), pp. 2036–2043.
23) Cicatelli, G. and Sieverding, C. H.: The Effect of Vortex Shedding on the Unsteady Pressure Distribution around the Trailing Edge of a Turbine Blade, *ASME J. Turbomach.*, **119** (1997), pp. 810–819.
24) Sondak, D. and Dorney, D.: Vortex Shedding in a Turbine Cascade, *Int. J. Turbo Jet Engines*, **16** (1999), pp. 107–126.
25) Manna, M., Mulas, M. and Cicatelli, G.: Vortex Shedding Behind a Blunt Trailing Edge Turbine Blade, *Int. J. Turbo Jet Engines*, **14** (1997), pp. 145–157.
26) Sieverding, C. H., Richard, H. and Desse, J.: Turbine Blade Trailing Edge Flow Characteristics at High Subsonic Outlet Mach Number, *ASME J. Turbomach.*, **125** (2003), pp. 298–309.
27) Sieverding, C. H., Ottolia, D., Bagner, C., Comadoro, A., Brouckaert, J. F. and Desse, J.: Unsteady Turbine Blade Wake Characteristics, *ASME J. Turbomach.*, **126** (2004), pp. 551–559.
28) El-Gendi, M. M., Ibrahim, M. K., Mori, K. and Nakamura, Y.: Numerical Simulation of Trailing Edge Vortex Shedding in a High Subsonic Turbine Cascade, Proceedings of JSASS-KSAS Joint International Symposium on Aerospace Engineering, 2007, pp. 8–11.
29) Sieverding, C. S., Cicatelli, G., Desse, J. M., Meinke, M. and Zunino, P.: Experimental and Numerical Investigation of Time Varying Wakes behind Turbine Blades, *Notes Numer. Fluid Mech.*, **67** (1999).
30) Spalart, P. R., Deck, S., Shur, M. L., Squires, K. D., Strelets, M. K. and Travin, A.: A New Version of Detached-Eddy Simulation, Resistant to Ambiguous Grid Densities, *Theor. Comput. Fluid Dyn.*, **20** (2006), pp. 181–195.

Appendix

The speed of sound, c_∞, and density, ρ_∞, were calculated from inlet and exit boundary conditions and isentropic relations, and L is the characteristic length taken as 1.0 m.

$$T_\infty = T_{o1}\left(1 + \frac{\gamma - 1}{2} {M_{2,is}}^2\right)^{-1}$$

$$P_\infty = P_{o1}\left(1 + \frac{\gamma - 1}{2} {M_{2,is}}^2\right)^{\frac{-\gamma}{\gamma - 1}}$$

$$c_\infty = \sqrt{\gamma R T_\infty}$$

$$\rho_\infty = \frac{P_\infty}{R T_\infty}$$